NUMERICAL ANALYSIS OF TEMPERATURE FIELDS INSIDE NONSPHERICAL BUBBLES IN THE FINAL STAGE OF COLLAPSE

Akihiro Yasuda and Hiroyuki Takahira

Osaka Prefecture University, Sakai, Osaka, Japan

Abstract

The temperature fields inside a collapsing bubble near a plane rigid wall are investigated. We develop a numerical method based on the boundary element method combined with the finite volume method. In this method, the adaptive unstructured grids which are generated by Delaunay triangulation are used inside the largely deformable bubble to consider the heat transfer of the internal gas. We compare the present numerical results with those using structured grids. The result shows that the present method has sufficient accuracy to investigate the bubble motion. It is also shown that the present method can be applied to the analysis for the temperature fields inside tiny bubbles in which the thermal boundary layer is thick. Since the unstructured grids are more flexible for the regeneration and resizing of grids, the present method is applicable to the dynamics of toroidal bubbles by taking the thermal diffusivity of the internal gas into account.

1 Introduction

When a bubble collapses near boundaries, it deforms with translational motion. Especially near the rigid boundary, the liquid microjet threads the bubble in the collapsing phase. It is well known that the liquid microjet induces the material damage (Blake & Gibson 1987). The extremely high pressure and temperature fields generated around oscillating bubbles can be used for a new environment of chemical reactions (Suslick 1989). In ultrasonic medicine, the nonlinear dynamics of microbubbles are utilized as the contrast agent in order to emphasize the ultrasonic images (de Jong et al. 1991). To clarify the physical phenomena induced by the collapse or nonlinear oscillations of bubbles, many theoretical and numerical studies have been made so far (Plesset & Prosperetti 1977; Blake & Gibson 1987; Feng & Leal 1997). Although it is often assumed that the gas inside the bubble obeys the polytropic gas law, it is impossible to handle the bubble motion accurately without considering the heat transfer inside the bubble. Thermal damping plays an important role for the nonlinear bubble dynamics (see e.g. Prosperetti et al. 1988).

Takahira et al. (1995, 1998) studied the bubble motion near a plane rigid wall using the boundary element method (BEM) combined with the finite volume method. They showed that the thermal damping affects the bubble profiles. However, since the structured grids were used in their analysis, they could not handle the final stage of bubble collapse. The usage of structured grids has the following disadvantages: (i) it is difficult to increase or decrease the number of grids, (ii) the grid regeneration sometimes fails because of the large distortion of grids. On the other hand, Yuan & Prosperetti (1997) applied structured grids only near the bubble wall and calculated the bubble collapse when the thermal boundary layer near the bubble wall was much thin. However, their method can not be applied to the motion of tiny bubbles when the thermal boundary layer near the bubble wall is relatively thick to its radius.

The toroidal bubble dynamics is also important to analyze the physical phenomena induced by violent bubble collapse and the material damage due to the liquid microjet. Some researchers studied the motion of toroidal bubbles using the boundary element method (Best 1993; Zhang et al. 1993; Takahira et al. 1997). However, there have been no studies for the toroidal bubble dynamics considering the heat transfer inside the bubble.

In the present paper, we apply unstructured grids, which are flexible for the regeneration and resizing of grids, inside the large deformable bubble. The numerical accuracy is discussed by comparing the present

results with the results of Yuan & Prosperetti (1997) when the thermal boundary layer inside the bubble is thin. We show that the present method is applicable in analyzing the temperature field inside the tiny collapsing bubble in which the thermal boundary layer is thick. The dynamics of a toroidal bubble is also discussed.

2 Basic Equations

Let us suppose that an initially spherical gas bubble exists near a plane rigid wall. We will investigate the bubble motion when the surrounding liquid pressure increases stepwise. Our analysis has been done under the following assumptions:

(i) Compressibility and viscosity of the liquid are disregarded and the flow field in the liquid is irrotational.
(ii) The interior of each bubble consists of a noncondensable gas. The gas obeys the perfect gas law.
(iii) The internal gas pressure is uniform. Viscosity of the gas is disregarded.
(iv) Diffusion of the gas through the bubble surface is disregarded.
(v) Effects of condensation and evaporation are disregarded.
(vi) Thermal boundary layers are disregarded in the liquid. The liquid temperature is constant.

These are the same assumptions that were used by Takahira et al. (1995). Under these assumptions, the basic equations for the internal gas are given by

$$\frac{D\rho_g}{Dt} + \rho_g \left(\nabla \cdot \vec{u}_g\right) = 0, \tag{1}$$

$$\rho_g c_{pg} \frac{DT_g}{Dt} - \dot{p}_g = \nabla \cdot \left(\lambda_g \nabla T_g\right), \tag{2}$$

$$p_g = \rho_g \mathcal{R} T_g, \tag{3}$$

where t time, $D/Dt = \partial/\partial t + \vec{u} \cdot \nabla$, ρ the density, $\vec{u}$ the velocity, c_p the specific heat at constant pressure, T the temperature, p the pressure, λ the thermal conductivity, $\mathcal{R}$ the gas constant, and dot the differentiation with respect to time. The subscript g denotes the gas. The momentum equation is not required because of the assumption (iii). Equations (1) and (2) are combined into

$$\frac{\dot{p}_g}{\kappa p_g} + \nabla \cdot \left(\vec{u}_g - \frac{\kappa - 1}{\kappa p_g} \lambda_g \nabla T_g\right) = 0, \tag{4}$$

where κ is the specific heat ratio. When we introduce the velocity potential φ_g for the internal gas, Eq. (4) is rewritten as

$$\nabla^2 \varphi_g = \frac{\kappa - 1}{\kappa p_g} \nabla \cdot \left(\lambda_g \nabla T_g\right) - \frac{\dot{p}_g}{\kappa p_g}. \tag{5}$$

Equation (2) is also rewritten by using Eq. (3):

$$\frac{DT_g}{Dt} = \frac{\kappa - 1}{\kappa} \frac{T_g}{p_g} \{\nabla \cdot \left(\lambda_g \nabla T_g\right) + \dot{p}_g\}. \tag{6}$$

On the other hand, the basic equations for the liquid are given by

$$\nabla^2 \varphi_l = 0, \tag{7}$$

$$\frac{D\varphi_l}{Dt} - \frac{1}{2} |\nabla \varphi_l|^2 + \frac{p_l - p_\infty}{\rho_l} = 0, \tag{8}$$

where subscript l and ∞ denote the liquid and infinity, respectively.

The boundary conditions at the bubble wall are

$$\frac{\partial \varphi_g}{\partial n_g} = -\frac{\partial \varphi_l}{\partial n_l}, \tag{9}$$

$$\frac{D\varphi_l}{Dt} - \frac{1}{2} |\nabla \varphi_l|^2 + \frac{p_g - 2\sigma H - p_\infty}{\rho_l} = 0, \tag{10}$$

$$T_g = T_l \ (= T_\infty), \tag{11}$$

where $\partial/\partial n_g$ and $\partial/\partial n_l$ are the normal derivatives in which $\vec{n_g}$ and $\vec{n_l}$ are outward normal for the gas and liquid, respectively, σ is the surface tension, and H is the mean curvature.

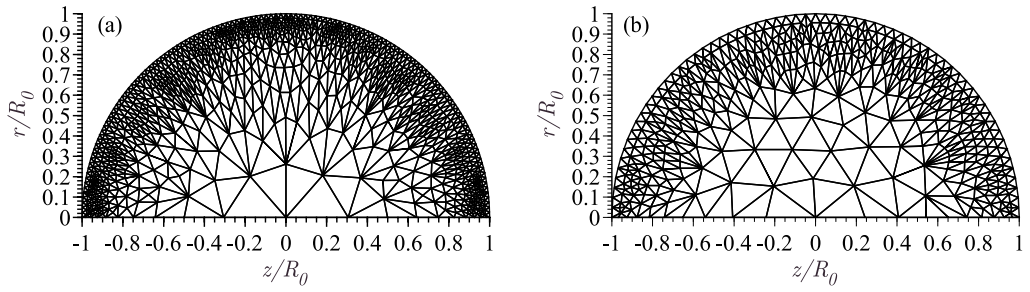

Figure 1. Initial computing grids.

3 Numerical Method

3.1 Outline of numerical procedure

In the first step, unstructured adaptive grids are generated by Delaunay triangulation (Taniguchi 1992) inside the bubble. In the present analysis, we need to concentrate the grids near the bubble wall to handle thermal boundary layers accurately. We use the grid adaptation method developed by Weatherill et al. (1994). This method makes the points concentrate near the source points. We put the source points on the bubble wall. We introduce the following point distribution function for each element generated by Delaunay triangulation:

$$d\zeta_j(x) = ae^{b|X_j - x|}, \tag{12}$$

where a and b denote the amplification and decay parameters of the source, respectively, X_j the position of each point source, x the centeroid of a triangle element. We define minimum value of $d\zeta_j(x)$ for each element as $d\zeta_{min}$. We calculate the distances d_v between the centeroid of the triangle element and each of three vertices. If $d\zeta_{min}$ is less than d_v, we insert a new point to the centeroid of the element. In this analysis, the values of a and b are selected so as to make $d\zeta_{min}$ small enough near the source points.

Figure 1 shows typical initial computing grids used in this paper. The z axis represents the axis of symmetry. For the calculation of Eq. (6), the cell volume per unit azimuthal angle is used. In Fig. 1 (a), a and b in Eq. (12) are taken to be 0.06 and 14.0, respectively, and the total number of elements is 1768. The bubble surface is divided into 128 boundary elements. While in Fig. 1 (b), the total number of elements is 790. The bubble surface is divided into 64 boundary elements.

In the next step, to get the bubble wall velocity, we solve the following boundary integral equation derived from Eq. (7):

$$\varphi_l(r,z) = \int_\Gamma \left(G_l \frac{\partial \varphi_l}{\partial n_l} - H_l \varphi_l \right) d\Gamma, \tag{13}$$

where

$$G_l = \frac{2r'}{\pi}\frac{K(k)}{\sqrt{A}}, \qquad H_l = \frac{2r'}{\pi}\frac{\partial}{\partial n_l'}\left(\frac{K(k)}{\sqrt{A}}\right), \qquad k = \sqrt{\frac{4rr'}{A}}, \qquad A = (r+r')^2 + (z-z')^2,$$

$$K(k) = \int_0^{\frac{\pi}{2}} \frac{d\theta}{\sqrt{1 - k^2 \sin^2\theta}},$$

$K(k)$ is the complete elliptic integral of first kind, Γ the cross section of the bubble surface cut by the half plane including the z axis.

The time derivative of the internal pressure is obtained from the integration of Eq. (4):

$$\dot{p}_g = -\frac{2\pi\kappa p_g}{V_b} \int_\Gamma \left(\frac{\partial \varphi_g}{\partial n_g} - \frac{\kappa - 1}{\kappa p_g} \lambda_g \frac{\partial T_g}{\partial n_g} \right) r d\Gamma, \tag{14}$$

where V is the volume of the bubble.

Then, the time derivative of the internal temperature is calculated from Eq. (6) by using the finite volume method. The temperature is constant inside each control volume.

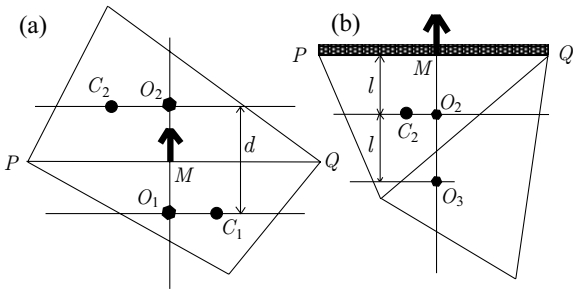

Figure 2. Calculation of normal derivative.

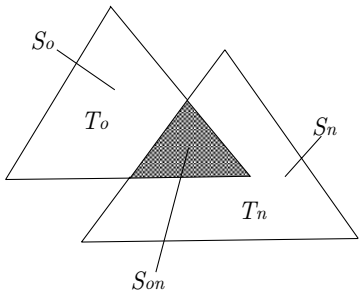

Figure 3. Calculation of temperature after grid regeneration.

The velocity potential of the gas at the bubble wall is calculated from Eq. (5). The internal gas velocity is obtained from the spatial derivative of Eq. (5) (Takahira et al. 1995).

After calculating all time derivatives, the location of the bubble wall, the velocity potential of the liquid side, the internal pressure, and the gas temperature are updated.

3.2 Evaluation of temperature gradient

The normal derivative of temperature through the surface between adjacent elements in Fig. 2 is calculated as follows. In Fig. 2 (a), the point C is the centeroid of an element and the point M is the midpoint between the points P and Q. d is the distance between the two lines that are parallel to $\overrightarrow{PQ}$ and pass the centeroids. The points O_1 and O_2 are located on the intersection between the line normal to $\overrightarrow{PQ}$ and the line parallel to $\overrightarrow{PQ}$. The temperature T_1 and T_2 are defined at the points O_1 and O_2, respectively. These temperatures are interpolated from the temperature of adjacent cells (Kobayashi et al. 1999). Using these values, the temperature gradient is given by

$$\frac{\partial T}{\partial n} = \frac{T_2 - T_1}{d}. \tag{15}$$

On the other hand, the temperature gradient on the bubble wall in Fig. 2(b) is calculated by the following equation:

$$\frac{\partial T}{\partial n} = \frac{3T_\infty - 4T_2 + T_3}{2l}, \tag{16}$$

where l denotes the distance between the points M and O_2. The point O_2 is on the line that is parallel to $\overrightarrow{PQ}$ and involves the centeroid C_2. The point O_3 is determined so that the point O_2 is located in the middle of the points M and O_3. The temperatures T_2 and T_3, which are the temperature at the points O_2 and O_3, respectively, are obtained from the same procedure as used for Fig. 2(a).

3.3 Grid regeneration

As the bubble deforms, the grid distortion occurs inside the bubble. Since the grid distortion decreases numerical accuracy, we must reconstruct the grids. When the liquid microjet threads the bubble, the steep temperature gradient arises in the narrow region on the z axis. In order to resolve the region near the z axis, the number of the internal elements must be increased or decreased according to the degree of the bubble deformation. When the grids are regenerated, the amplification and decay parameters of the source a and b in Eq.(12) are also changed according to the degree of the bubble deformation.

Temperature field after the grid regeneration evaluated by the following weight averaging form (Mavriplis 1988):

$$T_n = \sum_{new\ cell} \frac{T_o S_{on}}{S_n}, \tag{17}$$

where T_o is the temperature of the area S_o before resizing, and S_{on} is the intersection area between the area S_o and the area S_n that is regenerated after resizing (see Fig. 3).

3.4 Calculation of toroidal bubbles

After the liquid microjet threads the bubble, we use the boundary integral algorithm developed by Best (1993) to solve the Laplace's equation for the ambient liquid. Since the computational flow domain turns

into the toroidal form which is doubly connected after the liquid microjet impact, a cut τ is introduced to make the flow domain singly connected one. The discontinuity of the potential at the point of microjet impact, $\Delta\varphi$, which is equal to the circulation of the flow domain, is assumed to be constant in the present method. The governing equation for liquid around the toroidal bubble is given by

$$\varphi_l(r,z) = \int_\Gamma \left(G_l \frac{\partial \varphi_l}{\partial n_l} - H_l \varphi_l \right) d\Gamma - \int_{\Gamma_\tau} H_l \Delta\varphi d\Gamma. \tag{18}$$

To compute the internal state, the grids are regenerated inside the toroidal bubble. We interpolate the temperature field inside the toroidal bubble from the temperature field just before the impact. After determining the temperature fields, we calculate the toroidal bubble motion with the same numerical procedure as used before the impact.

4 Numerical Results and Discussions

4.1 Numerical accuracy

In this section, we discuss the effect of the total number of elements inside a bubble on the numerical results. We calculate the bubble collapse near a plane rigid wall. The initial radius and the initial distance between the bubble center and the rigid wall are $R_0 = 100\,\mu$m and $L_0 = 1.5R_0$, respectively. The initial gas pressure inside the bubble is $0.1p_\infty$. The liquid is assumed to be water at $T_\infty = 293.15\,$K and $\rho_l = 998.2\,$kg/m^3. The internal gas is air and its specific heat ratio κ is taken to be 1.4. The thermal conductivity is given by

$$\lambda_g = \alpha T_g + \beta, \tag{19}$$

where $\alpha = 5.28 \times 10^{-5}\,$W/mK^{-2}, $\beta = 1.165 \times 10^{-2}\,$W/mK (Prosperetti et al. 1988).

We use two kinds of mesh. The one is the mesh shown in Fig. 1 (a) (1768 elements) and the other is the mesh that involves 790 elements in Fig. 1 (b). Figure 4 shows the time histories of the bubble wall velocities at points N (north pole) and S (south pole). Figures 5 (a) and (b) show the temperature distributions inside the bubble at $t/t_0 = 1.124$ just before the microjet impact. In Fig. 4, the solid line represents the result obtained from the fine mesh (Case 1) and the dashed line represents that obtained from the coarse mesh (Case 2). Time t and velocity v are normalized by $t_0(= R_0/\sqrt{p_\infty/\rho_l})$ and $v_0(= \sqrt{p_\infty/\rho_l})$, respectively. Figures 5 (a) and (b) correspond to the results of Case 1 and Case 2, respectively. As seen from Fig.4, both results are in good agreement with each other. The coarse mesh used in Case 2 is sufficient to discuss the bubble wall velocity. On the other hands, comparing the temperature distributions inside bubbles, the temperature distribution in Fig. 5 (a) is smoother than that in Fig. 5 (b). The thermal boundary layer near the z axis in Fig. 5 (b) is overestimated. The overall nature is, however, captured correctly by the coarse mesh. We use the fine mesh in Fig. 1 (a) in the following computations.

Figure 6 shows the computing grids inside the bubble at $t/t_0 = 1.124$ in Fig. 5 (a). The grids near the z axis in Fig. 6 (a) are enlarged and shown in Fig. 6 (b). As seen from Fig. 6, the grids are concentrated enough near the bubble wall to consider the thermal boundary layer.

4.2 Comparison with the results by Yuan & Proseretti (1997)

We compare the present results with those of Yuan & Prosperetti (1997). They applied structured grids only near the bubble wall and assumed that the temperature was spatially uniform outside the grids.

Computational conditions are as follows. There exists an initially spherical bubble near a plane rigid wall at the ambient equilibrium pressure P_a (=1 atm). The bubble collapses after the pressure surrounding the bubble is suddenly overpressurized to $p_\infty = P_a + \Delta P$ (ΔP=10 atm). The initial radius and the initial distance between the bubble center and the rigid wall are taken to be R_0 =1 mm and L_0 =1.2 mm, respectively. The liquid surrounding bubble is Liquid Gun Propellant 1845 (ρ_l =1452 kg/m^3) and the undisturbed temperature is T_∞ =293.15 K.

The comparisons of successive bubble shapes and temperature distributions along the z axis are shown in Figs. 7 (a) and (b), respectively. Time shown in Fig. 7 (a) is normalized by $t_R(=0.915R_0\sqrt{\rho_l/\Delta P})$. In Fig. 7 (b), the solid line represents the present result and the dashed line represents the result calculated by Yuan & Prosperetti (1997).

Comparing bubble shapes in Fig. 7 (a), the present result is in good agreement with the result by Yuan & Prosperetti. As seen from Fig. 7 (b), since the initial radius is large, the thermal boundary layer becomes

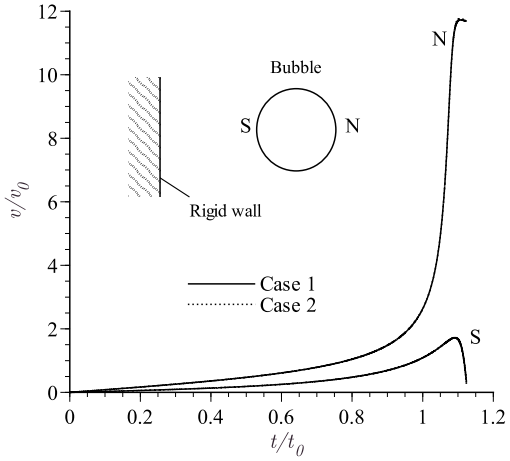

Figure 4. Comparison of time histories of bubble wall velocities.

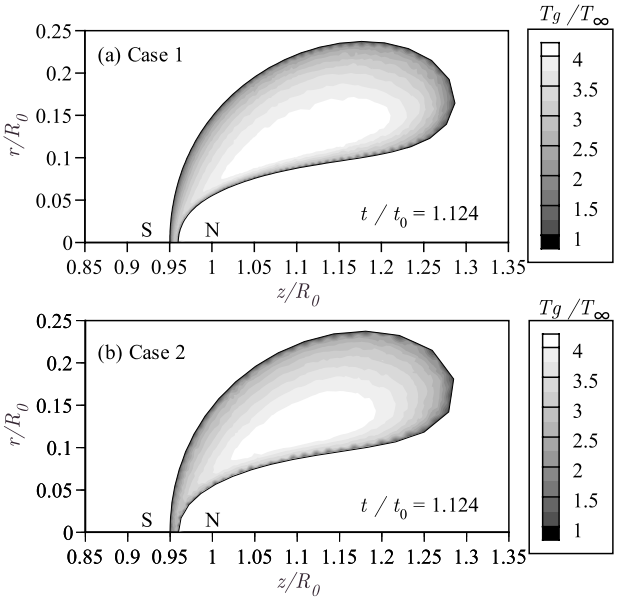

Figure 5. Comparison of temperature distributions.

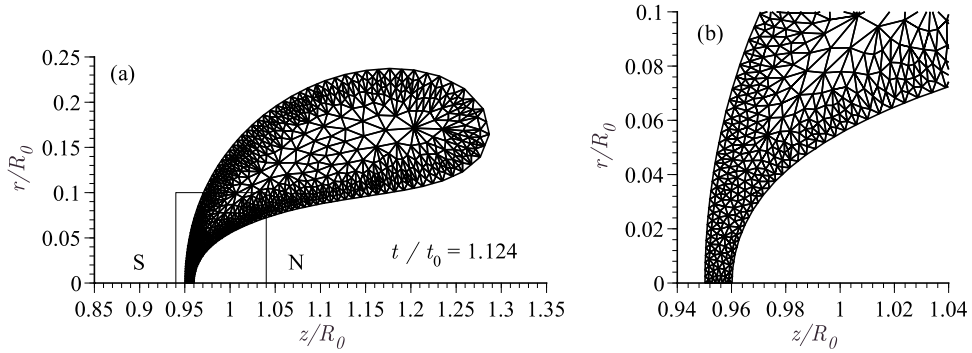

Figure 6. Computing grids inside the bubble at $t/t_0 = 1.124$.

much thin. It is also shown that the maximum temperature inside the bubble for the present method is 4% smaller than that for Yuan & Prosperetti. However, after the time (iv) in Fig. 7 (a), the temperature reaches about 1350 K in the present calculation. This minor difference may be due to the treatment of the thermal boundary layer. In the analysis of Yuan & Prosperetti, they assume the initial thickness of the thermal boundary layer. They also assume that the temperature field is spatially uniform outside the boundary layer. At the internal boundary of grids, they impose adiabatic boundary condition, which is given by

$$\mathbf{n} \cdot \nabla T = 0. \tag{20}$$

If the thickness of the boundary layer is evaluated thinner, the internal temperature may be overestimated. To consider the differences between two methods, the present result is in good agreement with the result by Yuan & Prosperetti. Therefore, the present method has sufficient accuracy to analyze the bubble motion in which the thermal boundary layer of internal gas is sufficiently thin to its radius.

4.3 Toroidal bubble

Since we generate mesh in the overall region for the internal gas, the present method has an advantage to handle the dynamics of tiny bubbles in which the thermal boundary layer becomes thick. Figures 8, 9 and 10 are typical results for the collapse of a tiny bubble when the initial radius R_0 is 50 μm. The other conditions are the same as those in Fig. 4. As seen from Fig. 8 (a), the bubble translates toward the rigid wall and the bubble surface deforms at the side furthest from the rigid wall. The liquid microjet threads the bubble at $t/t_0 = 1.109$ and the bubble evolves into the toroidal shape as shown in Fig. 8 (b).

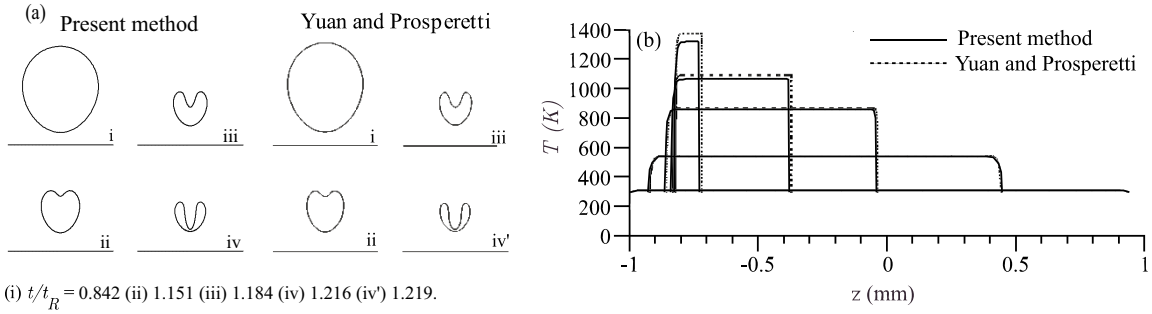

Figure 7. Comparisons of successive bubble shapes and temperature fields along the z axis.

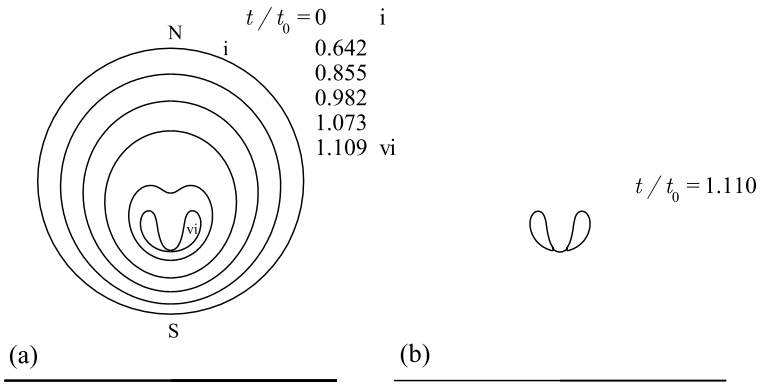

Figure 8. Successive bubble shapes when $R_0 = 50\,\mu$m, $L_0 = 1.5R_0$ and $p_{g0} = 0.1p_\infty$.

Figure 9 (a) shows the temperature field inside the bubble in the final stage of collapse at $t/t_0 = 1.109$. For comparison, the temperature field inside the bubble when $R_0 = 500\,\mu$m is also shown in Fig. 9 (b). The temperature T_g is normalized by T_∞. Since the thermal boundary layer inside a tiny bubble becomes thick, the thermal diffusivity affects the bubble motion strongly. As a result, when the initial radius is small, the internal pressure changes nearly isotropically. On the other hand, when the initial radius is large, the pressure changes adiabatically. As seen from Fig. 9, it is confirmed that the thermal boundary layer inside the bubble develops deeply inward. It is also shown that since the velocity of the bubble wall is accelerated by the thermal effects of the internal gas, the time of impact for $R_0 = 50\,\mu$m is earlier than that for $R_0 = 500\,\mu$m. It is also found from Fig. 9 that the thickness of the thermal boundary layer at the side N is thinner than that at the side S. This is because that the velocity of the bubble wall is much faster than that of the thermal diffusion at the side N.

Figures 10 (a) and (b) show the temperature field inside the toroidal bubble and the computing grids, respectively. As seen from Fig. 10, the temperature field inside the toroidal bubble can be analyzed with the present method using the unstructured grids.

5 Conclusion

We developed a numerical method that was based on the boundary element method combined with the finite volume method by using unstructured adaptive grids inside a bubble. The collapse of a bubble near a plane rigid wall was investigated by taking the heat transfer of the internal gas into account. We compared the present numerical results with those obtained by Yuan & Prosperetti (1997). The present results were in good agreement with those by Yuan & Prosperetti. The main conclusions are summarized as follows:

(i) The present method has sufficient accuracy to investigate the bubble motion when the thermal boundary layer inside the bubble is thin.

(ii) The present method is applicable to the dynamics of tiny bubbles in which the thermal boundary layer is thick.

(iii) The present method is effective in analyzing the internal temperature fields for toroidal bubbles in

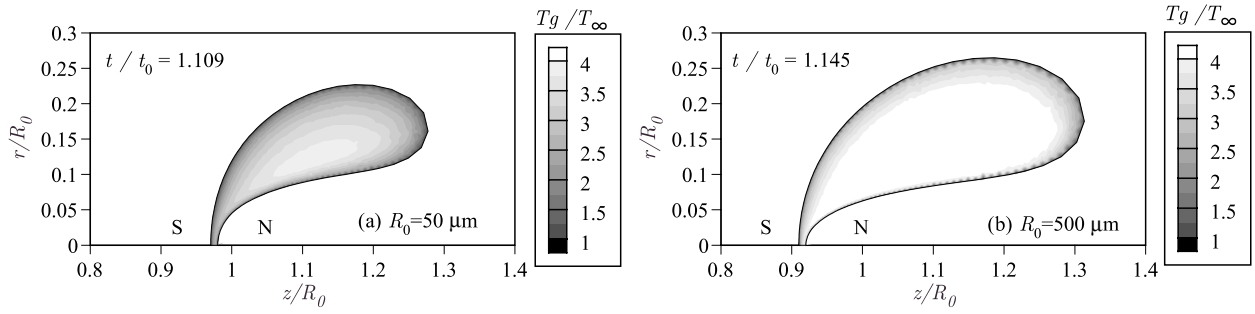

Figure 9. Internal temperature distributions just before microjet impact.

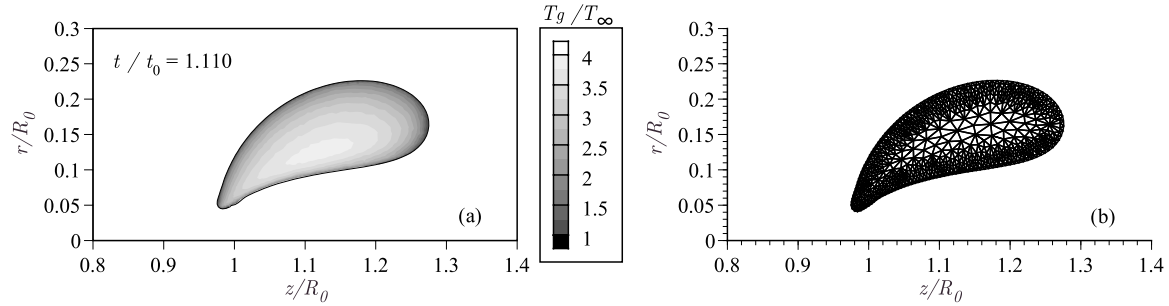

Figure 10. Temperature distribution and computing grids in the toroidal bubble.

the final stage of collapse.

References

Best, J. P. 1993 *J. Fluid. Mech.* **251**, 79-107.

Blake, J. R. & Gibson, D. C. 1987 *Ann. Rev. Fluid Mech.* **19**, 99-123.

de Jong, N., Ten Cate, F. J., Lancee, C. T., Roelandt, J. R. T. C. & Bom, N. 1991 Ultrasonics **29**, 324-330.

Feng, Z. C. & Leal, L. G. 1997 *Ann. Rev. Fluid Mech.* **29**, 201-243.

Kobayashi, M. H., Pereira, J. M. C. & Pereira, J. C. F. 1999 *J. Comput. Phys.* **150**, 40-75.

Mavriplis, D. J. 1988 *AIAA J.* **26**-7, 824-831.

Plesset, M. S. & Prospereeti, A. 1977 *Ann. Rev. Fluid Mech.* **9**, 145-185.

Prosperetti, A., Crum, L. A. & Commander, K. W. 1988 *J. Acoust. Am.* **83**-2, 502-514.

Suslick, K. S. 1989 *Scientific American*, February, 80-86.

Takahira, H., Miyamoto, H. & Akamatsu, T. 1995 *Proc. Cavitation and Multiphase Flow Forum, FED-Vol.210*, 173-179.

Takahira, H., Sakai, N. & Akamatsu, T. 1997 *Trans. Jpn. Soc. Mech. Eng.* B **63**-609, 1496-1504 (in Japanese).

Takahira, H. & Yasuda, A. 1998 *Proc. Third International Symposium on Cavitation, Vol.1*, 57-62.

Taniguchi, T. 1992 *Automatic Mesh Generation for FEM.* Morikita Shuppan (in Japanse).

Weatherill, N. P., Marchant, M. J., Hassan, O. & Marcum, D. L. 1994 *Int. J. Num. Meth. Fluids* **19**, 739-764.

Yuan, H. & Prosperetti, A. 1997 *Phys. Fluids* **9**-1, 127-142.

Zhang, S., Duncan, J. H. & Chahine G. L. 1993 *J. Fluid. Mech.* **257**, 147-181.